International Journal of Extreme Manufacturing

PAPER • **OPEN ACCESS**

Endowing low fatigue for elastocaloric effect by refined hierarchical microcomposite in additive manufactured NiTiCuCo alloy

To cite this article: Bo Feng *et al* 2024 *Int. J. Extrem. Manuf.* **6** 045501

OPEN ACCESS
IOP Publishing | IMMT
International Journal of Extreme Manufacturing
Int. J. Extrem. Manuf. **6** (2024) 045501 (16pp)
https://doi.org/10.1088/2631-7990/ad35ff

Endowing low fatigue for elastocaloric effect by refined hierarchical microcomposite in additive manufactured NiTiCuCo alloy

Bo Feng[1,6], Helong Liu[1,6], Ying Yang[2,*], Hui Shen[1], Yang Ren[3], Yinong Liu[4], Lishan Cui[1], Bingmin Huang[5] and Shijie Hao[1,*]

[1] College of New Energy and Materials, China University of Petroleum, Beijing 102249, People's Republic of China
[2] College of Chemical Engineering and Environment, China University of Petroleum, Beijing 102249, People's Republic of China
[3] Department of Physics, City University of Hong Kong, 83 Tat Chee Avenue, Kowloon, Hong Kong Special Administrative Region of China, People's Republic of China
[4] Department of Mechanical Engineering, The University of Western Australia, Perth, WA 6009, Australia
[5] Jiangsu Smart Advanced Material Tech Co., Ltd, Xuzhou 221000, People's Republic of China

E-mail: yyang@cup.edu.cn and haoshijie@cup.edu.cn

Received 11 December 2023, revised 16 January 2024
Accepted for publication 20 March 2024
Published 5 April 2024

Abstract

NiTiCu-based shape memory alloys have been considered as ideal materials for solid-state refrigeration due to their superb cycling stability for elastocaloric effect. However, the embrittlement and deterioration caused by secondary phase and coarse grains restrict their applications, and it is still challenging since the geometric components are required. Here, bulk NiTiCuCo parts with excellent forming quality were fabricated by laser powder bed fusion (LPBF) technique. The as-fabricated alloy exhibits refined three-phases hierarchical microcomposite formed based on the rapid cooling mode of LPBF, composed of intricate dendritic Ti_2Ni–NiTi composite and nano Ti_2Cu embedded inside the NiTi-matrix. This configuration endows far superior elastocaloric stability compared to the as-cast counterpart. The low fatigue stems from the strong elastic coupling between the interphases with reversible martensite transformation, revealed by *in-situ* synchrotron high-energy x-ray diffraction. The fabrication of NiTiCuCo alloy via LPBF fills the bill of complex geometric structures for elastocaloric NiTiCu alloys. The understanding of interphase micro-coupling could provide the guide for designing LPBF fabricated shape memory-based composites, enabling their applications for special demands on other functionalities.

[6] Both authors equally contributed to this work.
[*] Authors to whom any correspondence should be addressed.

Supplementary material for this article is available online

Keywords: NiTiCuCo, shape memory alloy, microcomposite, high-energy x-ray diffraction, laser powder bed fusion

1. Introduction

Elastocaloric cooling, one of the promising solid-state refrigerants, has attracted great interest recently [1–4]. It is viewed as a green alternative to traditional vapor-compression refrigeration that results in ozone-layer depletion [5–7]. The elastocaloric effect refers to the adiabatic temperature variation (ΔT_{ad}) of elastocaloric materials by the entropy change upon external stress [2, 4, 6]. For elastocaloric applications, in addition to the large ΔT_{ad} [6, 8, 9] and strong heat transfer [10, 11], durable fatigue resistance [6, 11, 12] is also vital for elastocaloric system.

The NiTi shape memory alloys (SMAs) are regarded as promising candidates for elastocalorics based on their remarkable ΔT_{ad} (up to 30 K) by large latent heat of reversible first-order martensite transformation [2, 13]. However, the ΔT_{ad} of most NiTi SMAs degrades appreciably in the course of cyclic stress due to the deterioration of martensite reversibility. Their functional fatigue originates from the accumulation of stabilized martensite, which is induced by either the initiation of irreversible plastic deformation under low strengths [14], or the interfacial friction by excessive structural distortions at transformation fronts [15, 16].

It is found that Ti-rich NiTiCu alloys by partial substitution of Ni by Cu in Ni–Ti exhibit superb stability up to a million times for elastocaloric cycles [16, 17]. Their underlying superior mechanisms for low fatigue are considered mainly results from the facts that (i) the excess substitution of Cu triggers the orthorhombic B19 martensitic transformation with lower thermal hysteresis rather than classical monoclinic B19′ martensite, reducing the energy dissipation of interfacial friction [9, 18, 19]; (ii) the presence of Ti_2Cu precipitates (under highly Ti-rich overall composition) provides epitaxial induction for transforming matrix and thus induces low energy pathway for each martensite transformation cycle [16, 20]; (iii) the nano-size grains strengthen the yield stress for dislocation slips to much higher than the critical stress for martensite transformation, avoiding the deterioration of martensite reversibility by plastic deformation [20, 21]. Nevertheless, recent advances are focused on the thin films fabricated by magnetron-sputtering. Restricted by the single geometric form, these films are not readily applied to large-volume and intricate geometries of elastocaloric system [5, 22, 23].

As for bulk NiTiCu alloys, the poor strength (coarse grain) and embrittlement are the fatal obstacles [20, 21]. Moreover, large-sized brittle Ti_2Ni intermetallic is also formed for both thin films and bulk Ti-rich NiTiCu community [16, 24–26]. It is recognized that the presence of Ti_2Ni phases is detrimental to the materials integrity since crack or fracture occurs owing to the local stress concentration [16, 27]. Therefore, it is difficult for the conventional bulk highly Ti-rich NiTiCu alloys to cold/hot work (cold deformation/refinement strengthening) that could improve the yield strength, or to machine the specific components with high elastocaloric transfer capability.

The laser powder bed fusion (LPBF) is well known for layer-by-layer control and endowing near-net-shape SMA parts with large surface areas for efficient heat transfer in elastocaloric devices [10, 28, 29]. In addition, the LPBF process has an ultra-rapid solidification of more than 10^4 °Cs^{-1} [30–32], which is tens of thousands of times more than that of conventional casting. Under such processing conditions, it is found that, for various metallic *in-situ* composites, the conspicuous refinement of multiphase grain size shows a promotion for mechanical performances [33–35]. This microstructural refinement is bound to rise soft-hard interfacial density dramatically. In NiTi-based composites fabricated by LPBF, the highly interphase match and conspicuous coupling exhibit strong interface-induced effect on the reversible martensite transformation [6, 8, 10]. Hence, it is expected that the LPBF fabricated NiTiCu alloys could demonstrate much smaller grain size than those of conventional counterparts, achieving microcomposite microstructure composed of elastocaloric transforming matrix and Ti_2Ni intermetallic phase. This configuration is expected to enlist strong coupling effect to improve elastocaloric cycling stability of transforming matrix. Furthermore, the transient annealing cycles under layer-by-layer printing conditions may result in the more uniformly dispersed nano Ti_2Cu phase rather than the conventionally precipitated along grain boundaries [21, 36]. This interspersion can further prompt the epitaxial induction on the transformation and contribute to enhancement of the elastocaloric reversibility.

In this study, we demonstrate the fabrication of geometric designable bulk NiTiCuCo alloy via LPBF. The little doping of Co is to bring down martensite transformation temperatures, enabling the elastocaloric effect to be obtained at ambient temperature with extremely low critical stress of transformation. Based on the rapid printing conditions, the refined hierarchical microcomposite is formed, composed of intricate dendritic Ti_2Ni-NiTi and nano Ti_2Cu embedded inside the NiTi-matrix, endowing a superior elastocaloric cycling stability at room temperature compared to the as-cast counterpart. The coupling phenomena between the phases and their evolutionary behavior upon B2 ↔ B19 martensite transformation are investigated by *in-situ* synchrotron high-energy x-ray diffraction (HE-XRD), revealing their mapping mechanisms to elastocaloric cyclic stability. This study provides a fundamental understanding of the interphase coupling micro-behaviour and

guidance for designing LPBF SMAs for applications with special demands on other functionalities.

2. Materials and methods

2.1. Sample preparation

Pre-alloyed powders with an atomic ratio of $Ni_{30.6}Ti_{54.4}Cu_{12.2}Co_{2.8}$ were obtained by gas atomization method from an as-casting bar. The particle size of pre-alloy powders used for LPBF is ranging from 18 μm to 66 μm, as shown in figure S1(a). The NiTiCuCo samples were fabricated by Eplus M100-T LPBF machine. The oxygen concentration of processing chamber was maintained below 100 ppm by an argon atmosphere. A stripe rotation strategy of laser scanning with hatch rotation of 67° and stripe width of 4 mm was implemented, as illustrated in figure S1(b).

To explore the forming qualities and optimal process parameters of LPBF-fabricated NiTiCuCo alloys, as shown in figure S1(c), cuboid-shaped samples with 4 mm (length) × 4 mm (width) × 6 mm (height) in dimension were fabricated under orthogonal parameter combinations, in which each sample had three replications to ensure the repeatability and reliability of the process. The forming qualities were characterized by inside cracks, lack of fusion, gas pores, keyhole pores, or microcracks, respectively. The corresponding forming quality morphology of optical micrographs (OLYMPUS DSX510) are shown in figure S1(d). Then the optimized formability map for NiTiCuCo alloys (figure S2(a)) was tailored by process parameter of scanning speed (m s^{-1}) and laser power (W) under fixed layer thickness (30 μm) and hatch spacing (70 μm).

The volumetric energy density (E_V) of each parameter combination was calculated and summarized in table S1. The optimal formability window is ranging from 111 J mm^{-3} – 125 J mm^{-3} for E_V, which is a narrow window compared to the binary NiTi groups [37–39]. Figure S2(b) shows the statistics of sphericities and diameters of all the pores inside one of the x-ray 3D CT (Yxlon FF85) samples with good formability (E_V = 119 J mm^{-3}, blue circle in figure S2(a)). The relative density is up to 99.98% according to the CT in inset of figure S2(b). It is found that the diameters of all the pores are less than 40 μm and the sphericities are higher than 0.5. These pore defects are dominated by tiny near-spherical gas-pores [38], while the large-sized keyholes or unfused pores are eliminated. The gas-pores are considered to have a negligible effect on the mechanical performance. Figure S2(c) shows a picture of LPBF NiTiCuCo parts with different heat transfer channel sizes fabricated by optimized process parameters, which can be used in solid-state refrigeration prototypes.

2.2. Performance tests

The as-fabricated cuboid NiTiCuCo samples with good forming quality were cut into cylinders with Φ3 mm (diameter) × 6 (height) mm in dimension by wire electric discharge for compression and elastocalorie tests. The compression tests were conducted by universal testing machine (Instron-5966) with strain rate of 10^{-3} s^{-1} at room temperature, in which a non-contacting video extensometer was performed to record the accurate strain. The elastocaloric associated temperature variation of the sample during compressive loading and unloading was monitored by the contact-type thermocouple and OM-DAQ-USB-2401 data acquisition module.

The transformation temperature was estimated by a TA Q20-2503 differential scanning calorimeter (DSC) with a cooling-heating rate of 10 K min^{-1}. As shown in figure S2(d), based on the Ti-rich attribute, the LPBF-NiTiCuCo alloy under various E_V has identical transformation temperatures, which is different from the extreme parameter sensitivity of that Ni-rich NiTi alloy reported [38, 40]. Therefore, for the parameter tuning of the AM NiTiCu-based alloys, there is no need to consider its influence on the transformation temperature and thus on the functional performances. The transformation type should be B2 ↔ B19 orthorhombic martensite transformation due to the doping of excess Cu, which will be further verified later. The reverse transformation finish temperature (A_f) is 282 K in DSC curves, indicating that the LPBF-NiTiCuCo alloy is superelasticity at room temperature. Based on the aforementioned narrow optimal forming window and identical transformation temperatures for the LPBF-NiTiCuCo, their microstructure and performance should be stable within the window. Therefore, the samples for performance tests and characterization were fabricated with the fixed energy density of 119 J mm^{-3}.

2.3. Microstructure characterization

The samples for microstructure observation were performed on scanning electron microscope (SEM, Zeiss G310), and transmission electron microscopy (TEM, Tecnai G^2 F20) at 200 kV equipped with a dispersive x-ray spectroscopy (EDS) detector and Gatan double-tilt holder. The TEM samples were prepared by mechanical polishing followed by twin-jet electro-polishing in an electrolyte of 25 vol% HNO_3 and 75 vol % CH_4O at 243 K and 30 V.

2.4. In-situ synchrotron HE-XRD

HE-XRD measurements were *in-situ* performed during compression deformation and cooling/heating on the 11-ID-C beam line of the Advanced Photon Source at the Argonne National Laboratory, USA. X-rays have an energy of 115 KeV, beam size of 0.5 mm × 0.5 mm and wavelength of 0.117 3 Å. Figure S3 depicts the schematic experiment for the *in-situ* HE-XRD measurement, where azimuth angle 90° represents the compressive loading direction, which is also the building direction of the LPBF-sample. For phase analysis, two-dimensional (2D) HE-XRD patterns were fully integrated (azimuth angle 0°–360°) to get 1D HE-XRD spectra using software Fit 2D, where a CeO_2 powder reference sample was used for calibration. Thereinto, 1D HE-XRD spectra along the loading direction were integrated at the azimuth angle within 90° ± 5°. The 1D diffraction peaks were fitted using Guass

distribution function to determine the peak area (diffraction intensity) and peak position (d-spacing values). The relative peak intensity rate is defined as $I_{hkl}/I^0_{hkl} \times 100$, where I_{hkl} and I^0_{hkl} are the integrated peak area under a given load or temperature and in the stress-free or original state, respectively. The d-spacing strain was calculated as $|d_{hkl}—d^0_{hkl}|/d^0_{hkl} \times 100$, where d_{hkl} is the d-spacing under a given load or temperature and d^0_{hkl} is the d-spacing in the stress-free state or original state.

3. Results

3.1. Micro-architectures of hierarchical composites

Figure 1(a) shows the SEM images of as-printed NiTiCuCo by LPBF. According to the backscattered electron contrast, the sample demonstrates separable two-phase dendrites. The statistical dendritic lamellar thickness (from three random SEM images) in figure 1(b) shows that the bright phase ($\sim$2 μm) is twice as large as that of the dark phase ($\sim$1 μm), implying that the volume fraction of the former is approximately twice as large as that of the latter. The phase constitutions of LPBF-NiTiCuCo was determined by Rietveld refinement method from its HE-XRD pattern at room temperature, as shown in figure 1(c). The sample is composed of three visible phases for B2, Ti_2Ni and Ti_2Cu with the volume fractions of 56.64%, 39.67% and 3.69% in figure 1(d), respectively. Thus, here phase transformable B2 matrix and hard Ti_2Ni phase are the main phase components. It is inferred that the bright contrast in SEM image is the B2 phase with a dominant volume fraction and the dark contrast is the Ti_2Ni phase, while Ti_2Cu phase is difficult to distinguish due to faint volume fraction and size.

In contrast, the as-cast NiTiCuCo alloy with the same element composition shows 10 times (10 μm–20 μm) lamellar thickness of the LPBF counterpart, despite their almost identical phase constitutions (figure S4). The significantly refined micro-architecture by LPBF is consistent with the expected one due to the rapid solidification processing environment [33]. The greatly refinement in LPBF sample arises significant interfacial density boosting, which presumably leads to the more pronounced composite coupling effect during deformation and confers remarkable enhancement in performances [34, 35]. In addition, under the nonequilibrium conditions of LPBF, the composite architecture exhibits short aspect ratios compared to the as-cast counterpart, endowing the integral microstructure and performance isotropized.

Figure 1(e) shows the microstructure of LPBF-NiTiCuCo in TEM, and the selected area electron diffraction (SAED) along the zone axis of $[111]_{B2}$ in figure 1(f) confirms the coexistence of NiTi-based B2 phase (BCC) and Ti_2Ni phase (FCC). According to EDS mapping in figures 1(g) and (h), the inter-dendritic belts tend to be segregated with Ti and exclusion with Ni, Cu and Co, confirming that the thinner is Ti-rich Ti_2Ni phase while Cu and Co are contained within B2 phases.

Inside the B2 grains, as shown in high-magnification bright-field image in figure 2(a), nano disk-like Ti_2Cu phase is dispersed with sizes varied from 10 nm to 20 nm in length and 2 nm to 5 nm in width along the zone axis of $[001]_{B2}$. Generally, the Ti_2Cu nano-disks strongly oriented within the B2 matrix and aligned perpendicular along the direction of $[100]_{B2}$ and $[010]_{B2}$ [25]. This is confirmed by the streaks along the $\{100\}_{B2}$ spots in SAED pattern of figure 2(b). The Ti_2Cu phase is precipitated under Ti-rich compositions condition (Ti $>$ 52.0 at.%) and grown from the disk-like Ti segregated G.P. zones [25], maintaining a high lattice compatibility with the matrix both B2 and B19 states [16]. The nano Ti_2Cu disks here are more dispersed than the conventionally precipitations [21].

Figure 2(c) shows a high-resolution TEM image of the representative NiTi (B2)–Ti_2Cu interface. Figure 2(d) shows the inverse fast Fourier transform (IFFT) image corresponding white dashed box in (c) by using the red circled spot in FFT pattern of its inset. In addition to the strain field contrast, the B2 and Ti_2Cu possessed good interface bonding and fully-coherent interface without mismatch; while the large-sized Ti_2Ni phase possessed semi-coherent interface and strained boundaries with B2 phases, and the interfacial dislocation and lattice distortion are shown in figure S5.

These results indicate that the LPBF-NiTiCuCo alloy has refined three-phase hierarchical microcomposite structures, that is, the NiTi (B2) and Ti_2Ni phase dendritic interlaced intricately at a submicrometer scale; the nano Ti_2Cu phase with disk-like shape is dispersed inside the B2 matrix and maintains a high degree of lattice coherence. This hierarchical microcomposite gives rise to phase interfaces under two scales, allowing homogenized interphases coupling with the transforming matrix.

3.2. Cycling performance for the elastocaloric effect

The cyclic elastocalorie of the LPBF-NiTiCuCo was tested by monitoring the temperature variation during compressive cycling. Figure 3(a) shows that the ΔT_{ad} of the sample is almost constant during the 400 cycling except for the first few decays. The heat-absorbing ΔT_{ad} of unloading is stabilized at 4.3 K after 400 cycles. Figure 3(b) shows corresponding stress-strain curves for 400 compressive cycles at room temperature. Here each cycle was compressed to a stress of 1000 MPa that exhibits optimal ΔT_{ad} values. Based on the insensitivity of the microcomposite structure to the strain rate [6, 10], the selection of the strain rate is also almost unlimited. The superelastic behavior changed and stabilized in the subsequent cycles after the first significant deterioration. For instance, the residual strain is maximum at the first cycle (about 0.86%) and then its increment decreases rapidly to zero, while the hysteresis loop area also decreases rapidly. Therefore, in practical applications, especially to ensure fatigue resistance, preliminary mechanical cyclic training is necessary to stabilize the reversability of phase transformation [6]. As a contrast, in figure 3(c), the ΔT_{ad} of the as-cast sample decayed to 1.8 K after only 100 cycles under the same experimental conditions, and could not be further cyclically deformed due to the large accumulation of residual strain. The specific micro-mechanical mechanisms of improved cycling stability for LPBF-sample will be elaborated later.

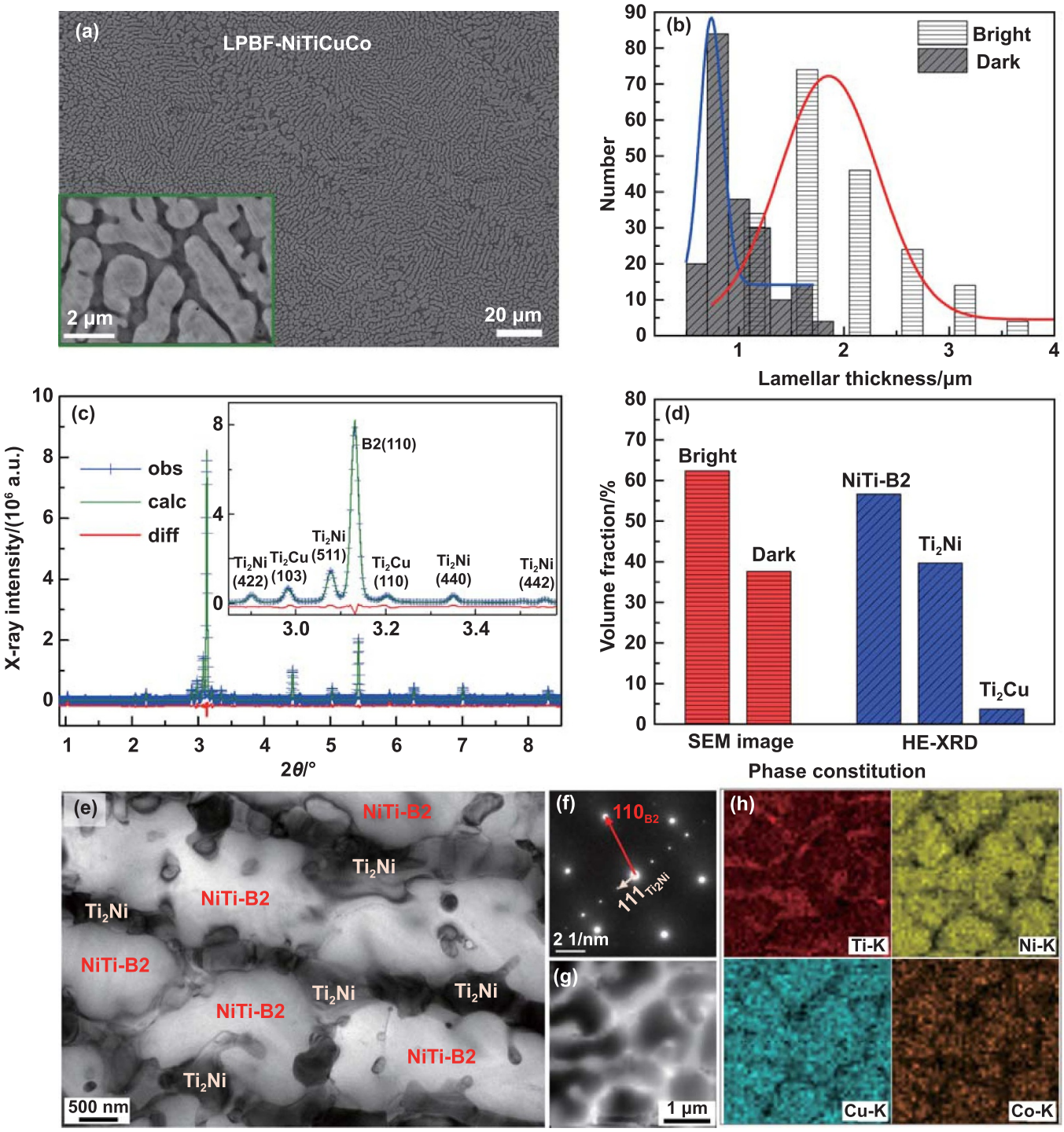

Figure 1. The constitutions and sizes of microcomposite in LPBF-NiTiCuCo sample. (a) SEM images of the sample under backscattered electron contrast. (b) Statistical dendritic lamellar thickness in both bright and dark contrasts at SEM images (data from three random images similar as (a)). (c) Rietveld refinement on HE-XRD pattern of sample at ambient temperature to determine the phase compositions. (d) Comparation of determined volume fractions from area ratio in SEM and refined results from HE-XRD. (e)–(f) Bright-field TEM image and selected area electron diffraction (SAED) pattern showing intricate dendritic structures composited by NiTi(B2) and Ti_2Ni phase. (g)–(h) EDX elemental mapping of dendritic structures.

Generally, for efficient elastocaloric cooling applications, in addition to the cycling stability, the SMAs are required to have superior comprehensive properties: (i) a large ΔT_{ad} (large output energy); (ii) a low critical superelastic stress (low input energy); (iii) as small a stress hysteresis as possible (low energy dissipation); (iv) large surface area or porosity (substantial heat exchange capability). Except that the fourth is achievable through additive manufacturing methods, the first three are responsible for the high elastocaloric efficiency (coefficient of performance, COP values) [6, 9]. The COP

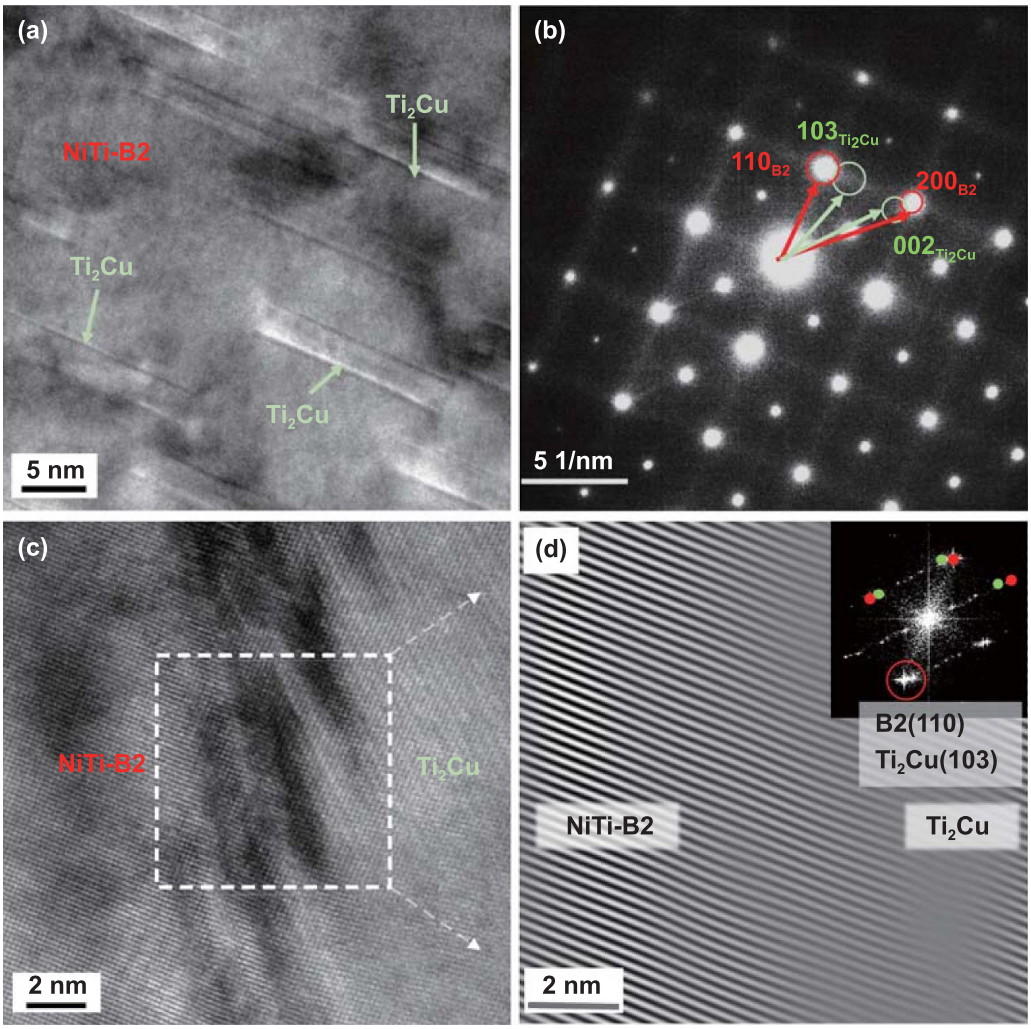

Figure 2. High magnification of TEM results shows nano Ti_2Cu phase inside the NiTi (B2) grains. (a)–(b) High magnification bright-field image and SAED along the zone axis of $[001]_{B2}$ showing the nano disk-like Ti_2Cu dispersed in the B2 matrix. (c) High-resolution TEM image NiTi (B2)–Ti_2Cu interface. (d) Inverse fast Fourier transform (IFFT) image of the interface from the red circled spot in the FFT pattern (inset; generated from the white dashed box in (c)).

is defined as the ratio of cooling power (ΔQ) to input work (ΔW), which is a parameter quantifying the refrigerating efficiency of material. The maximum COP value for the LPBF-NiTiCuCo in this study was calculated to be up to 19.6, which is a competitive value according to the results that have been summarized [21, 22].

3.3. In-situ micro-coupling behavior by the stress-induced transformation

To reveal the interphase coupling effect associated with stress-induced martensite transformation and elastocaloric effect for LPBF-NiTiCuCo alloy, the *in-situ* synchrotron HE-XRD measurement had been conducted during the compressive cycling. Figure 4 shows their cyclic micro-mechanical and coupling behavior upon three cycles compress to 1000 MPa. The evolution of 1D HE-XRD patterns integrated along the full Debye diffraction rings (azimuth angle 0°–360°) during compressive cycling is shown in figure S6. Figure 4(a) shows the evolution of 0°–360° integrated relative intensity rate of B2(100), demonstrating the process of stress-induced B2 ↔ B19 martensite transformation. The incomplete reverse of the B2 phase reflects that almost half of B19 martensite remains after the first cycle, corresponding to the residual applied strain in the stress-strain curve (figure 3(b)). Upon the subsequent cycling, homogeneous stress-induced transformation mode starts as soon as the loading is applied and the leftover B2 phase is transformed completely and fully reversible.

Figure 4(b) shows 1D HE-XRD patterns of lattice planes of each phase integrated at (90° ± 5)° (loading direction) during three compressive cycling. It is found that the diffraction peaks exhibit elastic shifts upon cycling, demonstrating the elastic deformation of each phase accompanied by stress-induced martensite transformation of NiTi-based matrix. Figure 4(c) shows evolution of B19(110) *d*-spacing strain during cycling. Since the B19 martensite is applied external stress as soon as it occurs, the corresponding original *d*-spacing in stress-free state ($d^0{}_{110}$) was obtained by the azimuth wave-crossing method. It is seen that the B19(110) lattice plane

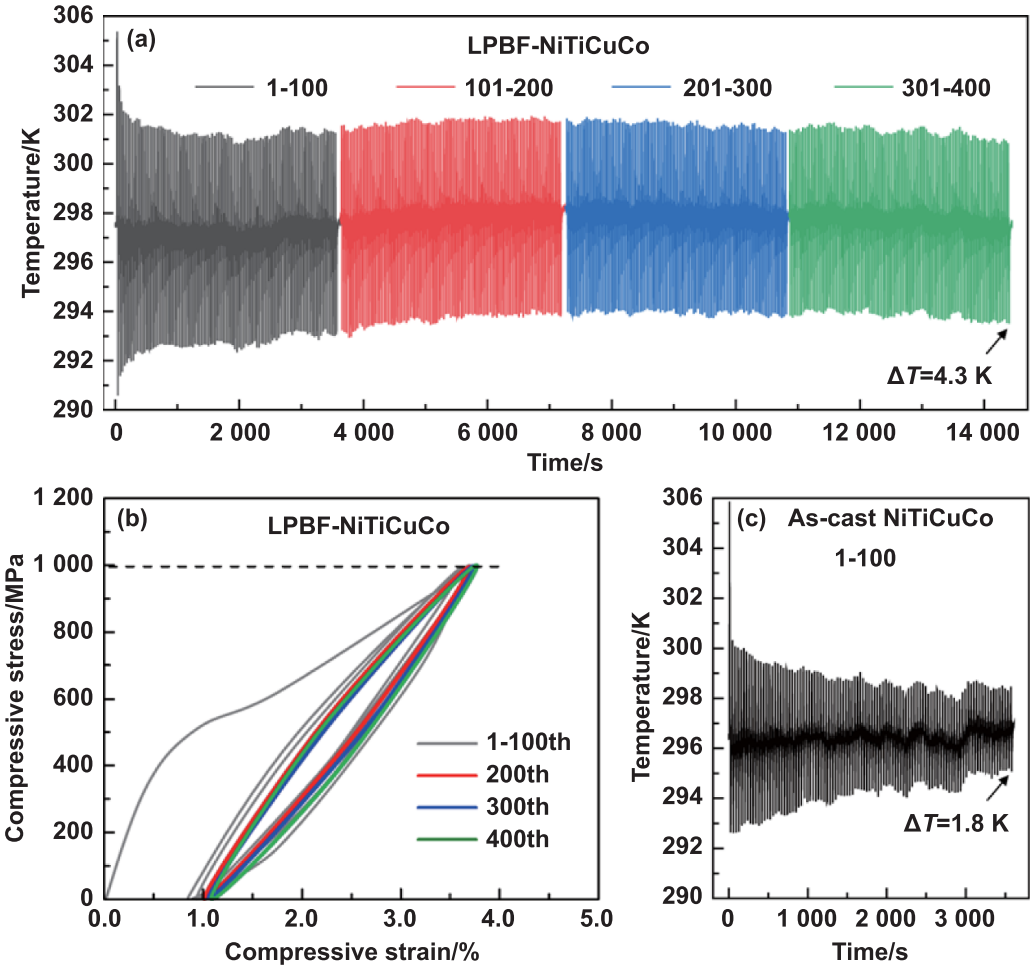

Figure 3. The cycling performance of LPBF fabricated and as-cast NiTiCuCo samples. (a) Elastocaloric temperature variation during the 400 loading-unloading cycling shown as a function of time. (b) Corresponding compressive stress-strain curves for 400 cycles. (c) As-cast NiTiCuCo during the 100 loading-unloading cycling. The loading and unloading rates are 2×10^{-2} s^{-1} and 5×10^{-2} s^{-1}, respectively.

is compressed once it appears, then instead in a tensile state (tensile *d*-spacing strain about 0.5%) after the first unloading, indicating that the residual martensite is subjected to an internal tensile stress along the loading direction [41, 42]. This internal stress field is fully reversible in subsequent cycling.

Figures 4(d) and (e) show the evolutions of *d*-spacing strains for untransformed $Ti_2Ni(111)$ and $Ti_2Cu(002)$ during cycling, respectively. In the first loading, both the *d*-spacing strains increase nonlinearly and display slightly sharp growth with the appearance of B19 martensite, which may correspond to the load transfer when the locally heterogeneous transformation frontier passing the x-ray beam detection point [43]. There is about 0.3% residual *d*-spacing strain for $Ti_2Ni(111)$ after first unloading, implying that a compressive stress field is left to Ti_2Ni phase along the loading direction. This compressive stress may be conjugate to the tensile stress field for B19 martensite in figure 4(c), which requires further confirmation, while the residual *d*-spacing strain of $Ti_2Cu(002)$ is negligible. In the subsequent cycling, the *d*-spacing strain of both phases is linear elastic reversible with applied strain.

Figure 4(f) shows the evolutions of full width at half maximum (FWHM) rate of untransformed $Ti_2Cu(002)$ and $Ti_2Ni(111)$ diffraction peaks upon three loadings. In the first loading, with the initiation of transformation in matrix (applied strain about 1.30%), the rates both phases increase sharply, and subsequently stabilize due to the completion of the transformation at the x-ray detection point, where the magnitude of the FWHM rate of $Ti_2Cu(002)$ is approximately twice that of $Ti_2Ni(111)$. The FWHM values of both phases only recover to about half of the maximum value after the first loading, while fully reversible in the subsequent loading. These evolutions are corresponding to the cyclic evolution of stress-induced B2 ↔ B19 martensite transformation in figure 4(a), reflecting the strong coupling heterogeneous effect caused by transformation [44]. For example, in the Ti_2Ni phase, as the stress-induced martensite transformation occurred, the outermost Ti_2Ni lattice near interfaces is first deformed by the adjacent shear of the transforming NiTi-based matrix, and then chain the inner Ti_2Ni lattice to move. In this case, the gradient of shear loading lead to strong strain heterogeneity along the loading direction of Ti_2Ni phase.

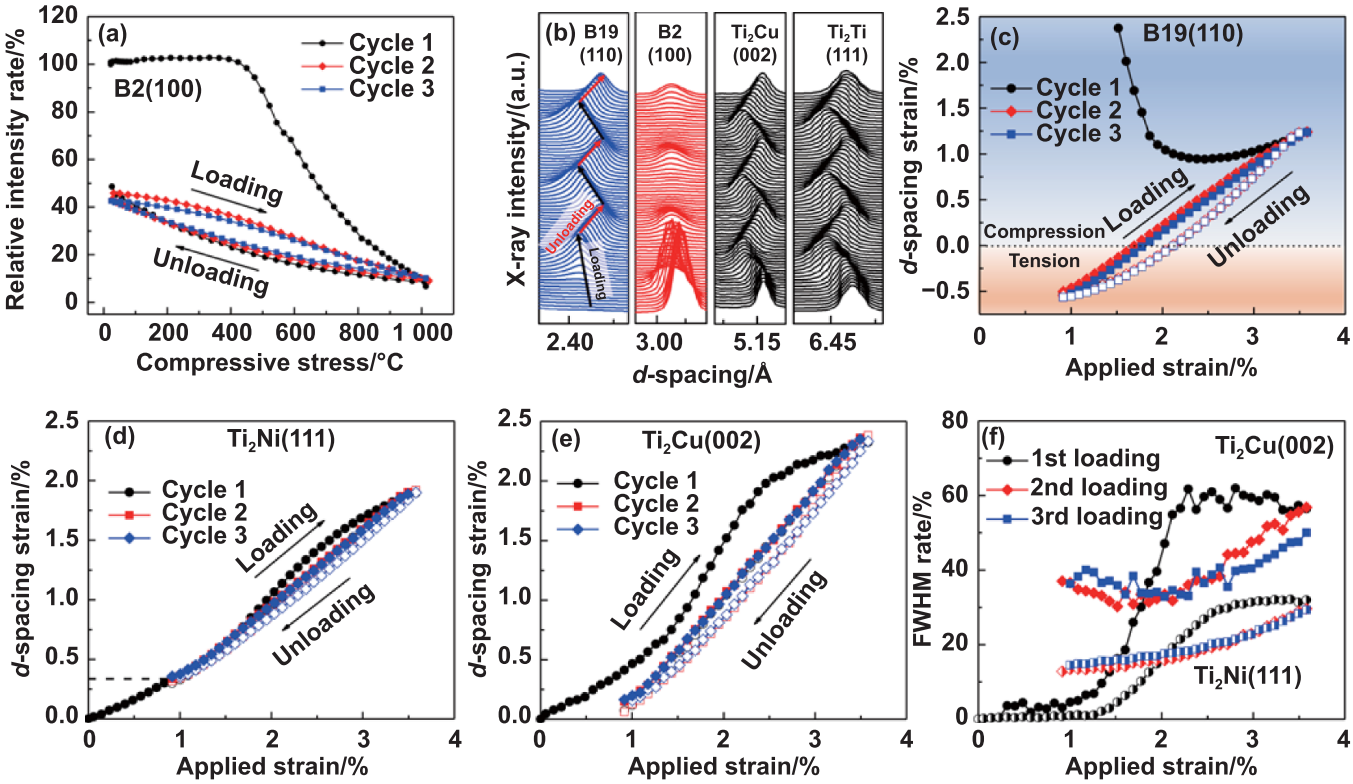

Figure 4. *In-situ* synchrotron HE-XRD results for cyclic micro-mechanical and coupling behavior upon three cycles compressed to 1000 MPa. (a) Evolution of 0°–360° integrated relative intensity rate of B2(100) upon three compressive cycles. (b) 90° integrated 1D HE-XRD patterns (loading direction) of lattice planes of each phase during cycling. (c) Evolution of *d*-spacing strain of B19(110) fitted from (b). (d) Evolution of *d*-spacing strain for $Ti_2Ni(111)$. (e) Evolution of *d*-spacing strain for $Ti_2Cu(002)$. (f) Evolutions of 90° integrated FWHM rate for $Ti_2Ni(111)$ and $Ti_2Cu(002)$ upon three loadings.

To study the overall stress coupling and strengthening effect of untransformed hard phases on the LPBF-NiTiCuCo composite, the loading partition between phases was analyzed. The component stresses of Ti_2Cu and Ti_2Ni phases are determined by

$$\sigma_{\mathrm{Ti2Ni}} = \varepsilon_{\mathrm{Ti2Ni(111)}} \cdot E_{\mathrm{Ti2Ni(111)}} \tag{1}$$

and

$$\sigma_{\mathrm{Ti2Cu}} = \varepsilon_{\mathrm{Ti2Cu(002)}} \cdot E_{\mathrm{Ti2Cu(002)}}, \tag{2}$$

respectively, where $\varepsilon_{\mathrm{Ti2Ni(111)}}$ and $\varepsilon_{\mathrm{Ti2Cu(002)}}$ are *d*-spacing strains from figures 4(d) and (e) that represent the elastic strains, $E_{\mathrm{Ti2Ni(111)}}$ (101.35 GPa) and $E_{\mathrm{Ti2Cu(002)}}$ (73.53 GPa) are elastic modulus in the normal direction of corresponding lattice plane calculated from compliance constants of a single crystal [45]. In the composite system of present study, the respective part stress (phase component load, σ_{appl}) borne by each phase under the total applied stress can be calculated by

$$\sigma_{\mathrm{appl}}(x) = \sigma_x \cdot \nu_x \tag{3}$$

where σ_x is the component stress of *x* phase from equation (1) or (2), ν_x is the volume fraction of *x* phase from figure 1(d) ($\nu_{\mathrm{Ti2Ni}} + \nu_{\mathrm{Ti2Cu}} + \nu_{\mathrm{trans\text{-}matrix}} = 1$). Since the matrix is transformable upon loading, the modulus difference between B2 and B19 phases results in component load that cannot be determined by equation (3), so the σ_{appl}(trans-matrix) of the matrix is obtained by:

$$\sigma_{\mathrm{appl}}(\text{trans - matrix}) = \sigma_{\mathrm{appl}} - \sigma_{\mathrm{appl}}(\mathrm{Ti_2Ni}) - \sigma_{\mathrm{appl}}(\mathrm{Ti_2Cu}) \tag{4}$$

where σ_{appl} is the global applied stress. The evolutions of component load for three phases upon the first cycle are shown in figure 5(a). In the initial stage (applied strain < 1.30%), each phase is purely elastic deformation mode, both Ti_2Ni and transformed matrix increase almost linearly. The Ti_2Cu phase bears much lower load than the former two due to its faint volume fraction. As the stress-induced transformation initiated (applied strain > 1.30%), the bearing load of matrix starts to decrease from 200 MPa, and bearing load for Ti_2Ni and Ti_2Cu continues to increase with a slightly higher growth rate, indicating that the load transfer occurs from the matrix to untransformed phase. Subsequently, the bearing load of matrix rises slightly while the growth rate of Ti_2Ni and Ti_2Cu slows down at the applied strain of about 2.50%, that is, the transform-finished matrix starts to deform elastically again but still much lower than the Ti_2Ni phase. Overall, under an applied load of 1000 MPa, the bearing load of Ti_2Ni phase is close to 800 MPa, while that of transformed matrix never exceeds 200 MPa. After unloading, there is a residual compressive stress about

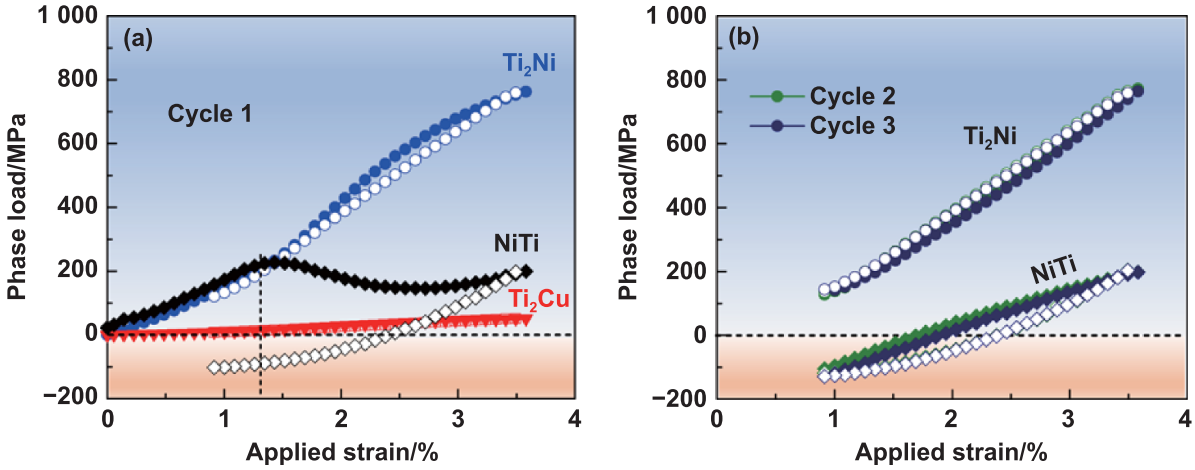

Figure 5. Evolutions of phase load of three components with cyclic applied strain, in which loading for solid plots and unloading for open plots. (a) First cycling. (b) Second and third cycling.

100 MPa for Ti_2Ni phase, on the contrary, the matrix exhibits reverse tensile stress about 100 MPa, verifying that the unrecovered martensite remains at the interface and mainly coupling with Ti_2Ni phase to form reciprocal stress field. In addition, the Ti_2Cu phase also remains very weak residual compressive stress relative to a small amount of martensite.

As shown in figure 5(b), in the subsequent cycles, the bearing load of matrix is always much lower than that of the Ti_2Ni phase, remaining about 1/4 of the latter and almost fully reversible during cycling. This demonstrates that the Ti_2Ni phase, accounts for 39.67% in volume fraction, can bear about 80% of the applied overall loading due to its intrinsic high strength, which exerts a significant enhancement on the overall mechanical properties.

Figure 6(a) shows the diffraction intensity distributions along the Debye ring of untransformed $Ti_2Cu(114)$ upon loading cycles. It exhibits obvious preferred reorientation during cycling, notably, the intensities along the loading direction (at 90°/270°) weaken while the intensities at 0°/180° and (0/180 ± 40)° intensify. In addition, this reorientation is fully reversible during the second and third cycling except for the partial reversibility of the first cycling, corresponding to the evolution of B2 ↔ B19 martensite transformation in figure 4(a). This indicates that, in addition to the intrinsic elasticity of the Ti_2Cu phase, it is accompanied by reorientation process [46]. As a comparison, in figure S7, the diffraction intensity of $Ti_2Ni(111)$ is almost stable during cycling at the same longitudinal coordinate scale, as well as for the other lattice planes of Ti_2Ni not shown here.

The overall elastic limit of Ti_2Ni along the compressive direction is about 2% (figure 4(d)), while it is known that the lattice shear strain exerted by martensitic transformation is up to 6% locally [42, 47]. This strain mismatch leads to the generation of coupled internal stress at the phase interface. In the coupling system of compressive loading, the transformed martensite with large shear strain is constrained by the Ti_2Ni phase with small elastic strain and subjected to inverted tensile stress, while the Ti_2Ni phase is subject to the corresponding compressive stress by martensite [42, 48]. After unloading, part of this coupling stress field is preserved due to the remain of nearly half of martensite that without reverse transformed back to the B2 phase, shown as the residual *d*-spacing strain in figures 4(c) and (d). On the other hand, there is no significant interphase coupling stress for Ti_2Cu due to its reoriented deformation that matches the strain difference with the lattice shear of martensite.

In thin NiTiCu film materials, it is considered that the Ti_2Cu nano-precipitates serve as sentinels to complete the reversible transformation in each memory cycle under the guidance of dual-epitaxies relationship with transforming matrix [16]. The lattice cell of dual-epitaxies relationship is illustrated in figure 6(b), that is, B2(100)//B19(011)//$Ti_2Cu(002)$, and B2(110)//B19(010)//$Ti_2Cu(103)$. Figures 6(c) and (d) show the azimuth orientation distribution of two lattice correspondences for three phases by external stress. It is seen that the spatial orientation distribution of Ti_2Cu before and after loading bears a resemblance to that of B2 and B19 phases, respectively. The little differentiation arises from the reorientation of B19 martensite and Ti_2Cu phase under external axial stress. The lattice mismatch strains of Ti_2Cu with the B2 and B19 phases after stress-induced transformation are 2.33% and −2.36%, respectively, indicating that the NiTi–Ti_2Cu phase interface is still fully coherent under external stress of 1000 MPa.

4. Discussion

In this work, a NiTiCuCo alloy with microcomposite was fabricated via LPBF, which exhibits low fatigue for elastocalorics at room temperature compared to its as-cast counterpart. The extreme printing conditions of LPBF endow the refined hierarchical microcomposite structures. This configuration and its composite effect must obey strict mapping mechanisms with excellent apparent performances. To provide insight into the

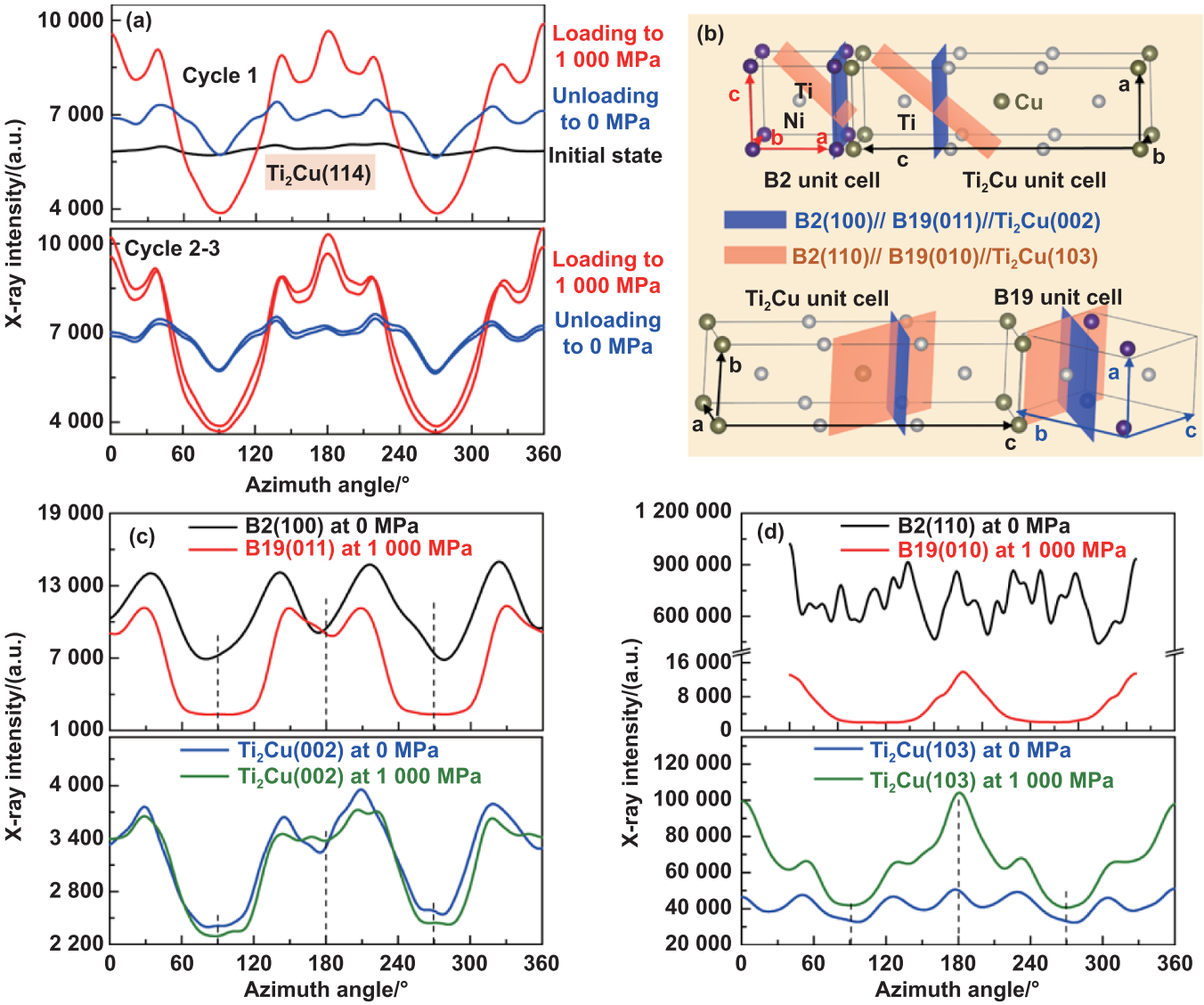

Figure 6. Concomitant deformation and epitaxial behaviors of the Ti_2Cu phase relative to the martensitic transformation. (a) Diffraction intensity distribution of untransformed phases $Ti_2Cu(114)$ along the fully azimuth angle from 0° to 360° during compressive cycling. (b) The lattice structure displaying parallel lattice planes and epitaxial relationship between Ti_2Cu phase and transforming B2 and B19 phases. Comparison of diffraction intensity distribution of (c) B2(100) and (d) B2(110) with their lattice corresponding B19(011) and B19(010), and $Ti_2Cu(002)$ and $Ti_2Cu(103)$, respectively, along the fully azimuth angle during the stress-induced transformation.

origin of fatigue resistance, it is primary to understand the contributions of the various enhancement mechanisms.

4.1. Refinement effect by LPBF

The LPBF-NiTiCuCo sample exhibits excellent cycling stability for elastocaloric effect (figure 2) compared to the as-cast sample despite their identical element and phase compositions. Thus the improvement originates from a tenfold difference in grain size (figures 1 and S4). It is known that the LPBF technique involves rapid solidification rate from ultrahigh temperature with transient heat cycling, resulting in microstructures different from conventional casting at multiscale [30, 49, 50]. On the one hand, the size scale of the microstructure is inversely correlated with the solidification rate, in which at least four orders of magnitude higher in LPBF than that of casting [6, 37]. Unless single-phase alloys grow into coarse columnar grains by multi-pass remelting [33, 51], some polyphase composites (e.g. eutectics) are significantly inhibited from migrating of the boundaries at high supercooling by additive manufacturing, leading to ultra-fine microcomposite at a submicro- or nanometer scale [36, 37, 52, 53]. On the other hand, the instantaneous high energy input and sharp temperature gradient (10^6 K m^{-1}) bring in the perturbation and contraction of the solid–liquid interface at high surface tension driven by the Marangoni effect inside the melt pool [6, 37], resulting in intricate interfaces and small aspect ratio compared to the as-cast sample (figures 1 and S4).

Following the generalized Hall–Petch relationship, grain refinement is considered to be one of the most effective

thoughts for strengthen metallic materials [54, 55]. Minishing the average grain size boosts a higher density of grain boundaries, which serve as strong pinning points to hinder the dislocation slip and improve the yield strength [48, 56]. For SMAs, the improvement of yield strength also avoids the stabilization of martensite by dislocation accumulation, thus enhancing the overall cycling stability for transformation. This is verified by the low strength of as-cast sample with much coarse grain size, which is continuously introduced to plastic deformation during cycling, deteriorating the transformation reversibility until the disappearance of the elastocaloric effect in figure 3(c). It is noted that the plastic deformation here is not only the transformed matrix, but the coarse secondary phase that also inhibits the transformation due to the release of the elastic strain energy [42].

In the NiTi-based composites that matrix is lattice-shear deformed by transformation, the load-bearing phase not only brings in strong back stress field at the interface to resist dislocation movement [47, 57], but also exerts elastic interaction with matrix that may promote the martensitic transformation [10, 43]. Furthermore, as the phase sizes are reduced and interfacial densities are boosted, the elastic coupling between the phases would be improved significantly, acquiring a synergistic enhancement on elastocaloric effect. Hou *et al* considered that the coupling effect in additive manufactured microcomposite receded the stress hysteresis of transformation greatly, and then endowed ultra fatigue-resistance for elastocaloric effect [6, 8]. The refined hierarchical microcomposite structures in LPBF-NiTiCuCo similarly induced highly matched interfaces as well as significant micro-coupling with the transformation, contributing to their excellent elastocaloric stability. This is detailed in the following section.

4.2. Reinforcing and coupling of Ti_2Ni phase

The interdendritic Ti_2Ni phase with high elastic modulus (up to 141 GPa) and intrinsic high strength is the main load-bearing component of the microcomposite during deformation. As shown in figure 5, the Ti_2Ni phase with 39.67% of the volume fraction can bear 80% of the overall external load, protecting the transforming matrix with major volume fraction from overloading and irreversible plastic deformation. In addition, the high-density curved interfaces rise remarkable back stress as a major obstacle to resist dislocation motion. Therefore, first of all, Ti_2Ni phase is the dominant reinforcing component to enhance the overall strength of the material in present composite system.

In another sense, according to the HE-XRD results in figure 4, almost half of the martensite remains at the Ti_2Ni interface after the first cycle, forming strong coupling stress field. This coupling effect after the first deformation alters the martensite transformation mode from a critical local launch-type to a homogeneous type, in which the latter exhibits a far lower transformation barrier and stress hysteresis [6, 8]. To further verify this mechanism, the microstructure after three compressive cycles was observed by TEM, as shown in figure 7(a), residual B19 martensite laths and some deformation dislocations do exist at the NiTi–Ti_2Ni interface. The tips of the martensite laths point to the interior of the transformable matrix, implying that martensite propagation initiated from the interface motivated by coupling stress. Figure 7(b) shows the corresponding SAED of NiTi-based matrix near interface along the zone axis of $[001]_{B2}$ ($[010]_{B19}$). It is seen that the mutation of the spots indicates the superposition of the B2 and B19 phases, confirming the coexistence of the highly lattice-compatible B19 martensite and the B2 parent phase [16]. Inside the transformable matrix, as shown in figure 7(c), the reverted B2 phase exhibits clear track lines left by stress-induced B19 martensite transformation process. During each cycling, the residual martensite is propagating along these tracks strictly, ensuring the reversibility and integrity of the transformation.

The schematic diagram of the microcomposite during first compressive loading is shown in figures 7(d)–(f). After the first compression to 1000 MPa and unloading, a high density of B19 martensitic laths and coupling stress fields is remained at the Ti_2Ni-matrix interface. The intricate network formed via LPBF enlists the deformed sample with uniformly dispersed interfacial martensite and coupling stress fields, which can serve as nucleation points and driving forces for stress-induced martensitic transformation during subsequent cycling, respectively. For one, this micro-configuration divides the B2 $\leftrightarrow$ B19 transformation frontier infinitely, reducing the fronts meet and frictional work [6]. Moreover, the nucleation barrier for transformation is eliminated, allowing the transformation to initiate at very low applied loads, as shown in figure 4(a), where the transformation starts as soon as stress is applied. Under the guidance of elastic coupling of Ti_2Ni at interface (evolution of the FWHM rate in figure 4(f)), the transformation process propagates as homogeneous and stable as possible along the interface, reducing the irreversible energy dissipation by transformation. The above factors promote small hysteresis and high transformation completeness effectively, which enhance the fatigue resistance for elastocaloric effect. In addition, compared to other NiTi-based hard nonequiatomic phases (e.g. Ni_3Ti or Ni_4Ti_3), the Ti_2Ni phase has an ultrahigh heat capacity (for the output energy), which helps to exhibit a much higher COP values of elastocaloric effect [10].

4.3. Epitaxy and coupling of Ti_2Cu phase

In the stress-induced transformation, as discussed in section 4.2, the dominant initiation of transformation upon cycles originates from the residual martensite at the Ti_2Ni interface, while the Ti_2Cu phase with faint volume fraction exhibits the transformation epitaxy shown in figures 6(c) and (d). The issue here is the inability to embody the individual promotion of Ti_2Cu to cyclic stability of reversible transformation upon external loading. Thus, considering there is no interaction for larger and harder Ti_2Ni phase under loading-free, the *in-situ* HE-XRD measurement has been conducted during the heating and cooling process, as shown in figure 8(a).

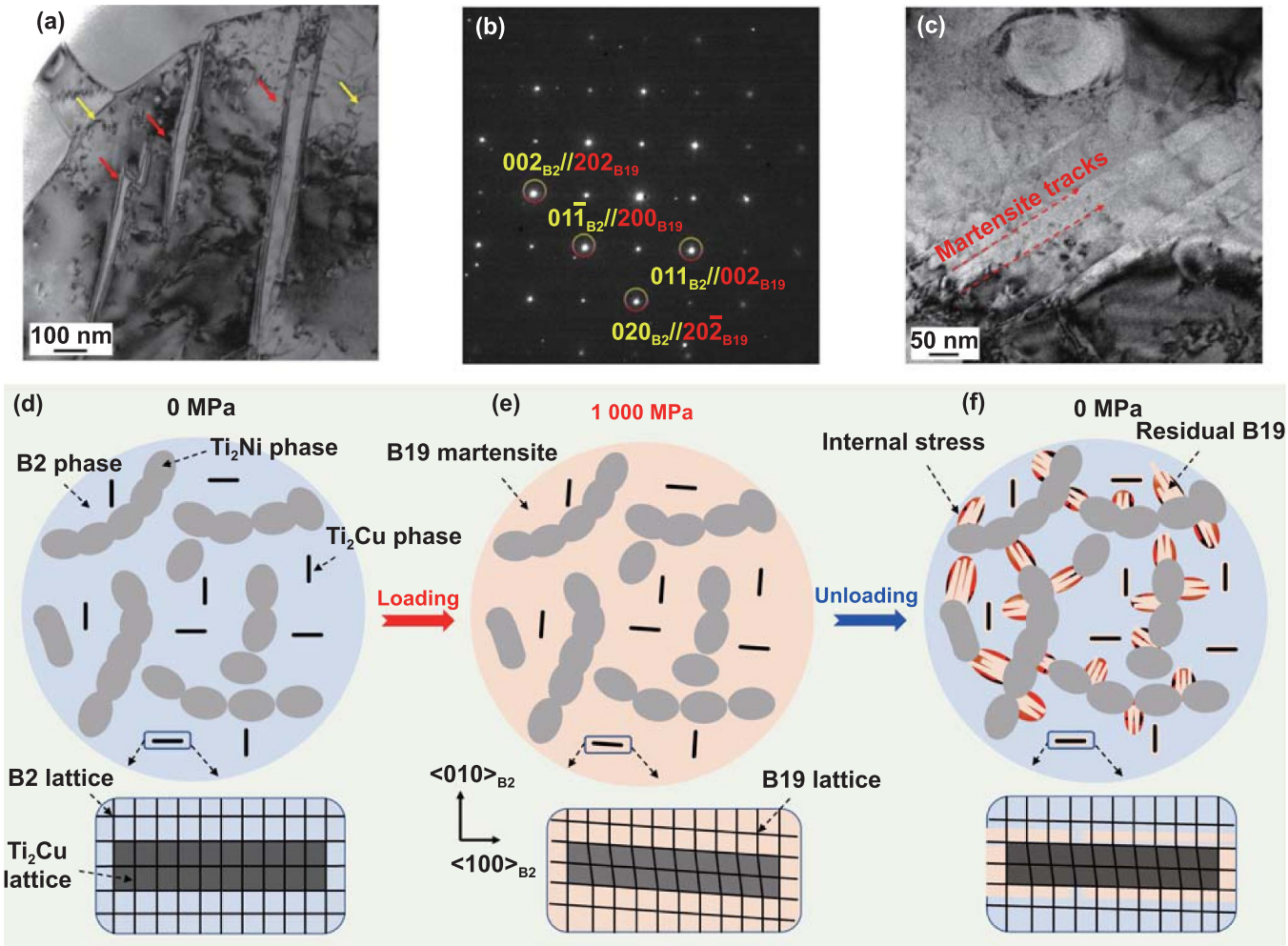

Figure 7. Formation and diagram of interfacial residual martensite. (a) Residual B19 martensite laths (red arrows) and deformation dislocations (yellow arrows) at the NiTi–Ti_2Ni interface in the TEM bright-field image after three cycles. (b) The SAED spots of the matrix near interface after deformation is the superposition of the B2 and B19 phases along the zone axis of $[001]_{B2}$ ($[010]_{B19}$). (c) Track lines of the B19 martensite transformation progress within the B2 matrix. (d)–(f) Schematic representation of the 2D evolutions of multiphase coupling during the first compressive cycling.

During the thermal-induced B2 ↔ B19 martensite transformation process (figure 8(b)), it is primarily the Ti_2Cu phase interact elastically with the transforming matrix, while it is difficult to drive the Ti_2Ni phase without external stress (figures 8(c) and (d)). In this case, the martensite transformation peaks also exhibit perfectly overlapping after 20 thermal cycles of using DSC measurement, as shown in figure S8. This thermal fatigue resistance is rare to achieve for classic binary NiTi alloys that generally show a gradual shift to lower temperatures as the defects accumulate during thermal cycling [58].

It is known that the Ti_2Cu phase exhibits extreme low lattice mismatch strain and specific orientation with both B2 and B19 phases [16], which are also shown in the figures 8(e) and (f). This superior compatibility endows the dual-epitaxial growth for both the forward and reverse martensite transformation along the Ti_2Cu interface, which is verified by the highly crystallographic inheritance relationship between the Ti_2Cu and corresponding B2/ B19 phase. In other words, the B19 martensite and B2 parent phase initial and grow from the Ti_2Cu lattice epitaxy, respectively. The combination of dual epitaxy of Ti_2Cu and small hysteresis of B19 transformation is the essential mechanism of excellent cycling stability for thermal-induced transformation in figure S8. Therefore, during the stress cycling, in addition to the dominant Ti_2Ni phase, part of the transforming matrix is also epitaxially grown from the Ti_2Cu phase interface. This epitaxial growth not only ensures the reproducibility and completeness of the transformation, but also further promotes the heterogeneity of transformation as discussed in 4.2, contributing to the cycling of the elastocaloric effect.

For the deformation mode of Ti_2Cu phase during stress-induced phase transformation, as shown in figure 6(a), it is not purely elastic-plastic deformation path as the typical precipitations, but accompanied by reorientation-like deformation. The schematic illustration of the micro-deformation process of Ti_2Cu is shown in the lower part of figure 7. The Ti_2Cu lattice keeps fully coherent with the B2 lattice before deformation due to their nano size and strict orientation figure 7(a). After loading (b), in addition to intrinsic elasticity, the Ti_2Cu disk reorients following the lattice shear of

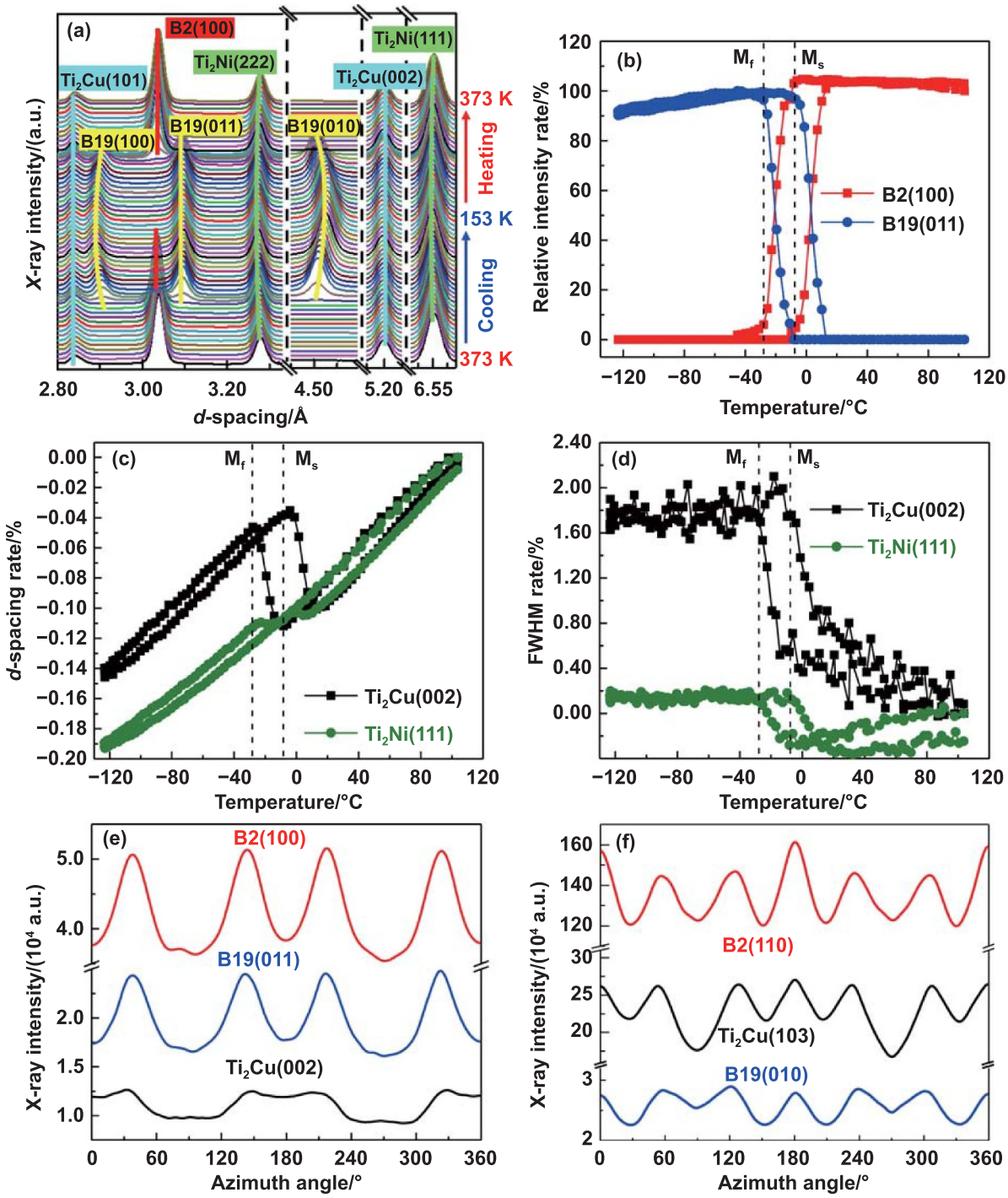

Figure 8. *In-situ* synchrotron HE-XRD results of LPBF-NiTiCuCo sample for thermal-induced micro-coupling behavior upon cooling and heating. (a) Evolution of 1D HE-XRD patterns integrated along the full Debye diffraction rings (azimuth angle 0°–360°) during one thermal cycling. (b) Evolution of 0°–360° integrated relative intensity rates of B2phase (B2(100)) and B19 martensite (B19(011)) fitted from (b). (c) Evolution of *d*-spacing strains for $Ti_2Ni(111)$ and $Ti_2Cu(002)$ phase. (d) Evolution of FWHM rates for $Ti_2Ni(111)$ and $Ti_2Cu(002)$ phase. (e)–(f) Distribution of diffraction intensity of B2(100) and B2(110) with their lattice corresponding B19(011) and B19(010), and $Ti_2Cu(002)$ and $Ti_2Cu(103)$, respectively, along the full Debye rings (azimuth angle 0°–360°).

martensite growth rather than hinder martensite shear like in typical precipitations, maintaining the overall interphase lattice match. After first unloading (c), the reorientated lattice of the Ti_2Cu is partly reversed by the reverse transformation, but it cannot be fully reversed to the initial state due to the coupling of the faint residual martensite at the interface (partially reversible of the orientation in figure 6(a)). During the subsequent cycling, the deformation strain magnitude of Ti_2Cu phase matches the large local lattice strain (∼7%) of B19 martensite transformation and always keeps the fully lattice-coherence, ensuring epitaxial growth of the stress-induced transformation.

At present study, in addition to the secondary phase, due to the excess solution of Cu atoms in the matrix, the B19 martensite shows an intrinsic small transformation hysteresis based on its high lattice compatibility with the B2 phase. The middle eigenvalue (λ) in this study is 0.9895 evaluated by using the lattice parameters extracted HE-XRD data, which is very close to the ideal value ($\lambda = 1$), suggesting the good geometric compatibility between B2 and B19 lattice [9, 15, 16]. The high lattice compatibility can alleviate the misfit strains and dislocations at the martensite transformation frontier, and thus reduce the dissipated frictional energy, accounting for low hysteresis and good reversibility of the elastocaloric effect.

5. Conclusion

In this work, a NiTiCuCo alloy with refined hierarchical microcomposite was fabricated by LPBF, exhibiting much superior cyclic stability for elastocaloric effect at room temperature than as-cast counterpart. The following conclusions are drawn:

(1) The LPBF-NiTiCuCo shows refined composite grain sizes under the ultrafast cooling conditions, about one-tenth of that as-cast counterpart. Highly-refined hierarchical microcomposite structures are achieved composed of intricate dendritic Ti_2Ni-NiTi and nano Ti_2Cu embedded inside the NiTi-matrix, endowing a superior cyclic stability for elastocaloric effect.
(2) The intricate fine Ti_2Ni phase is the dominant load-bearing phase (80% of the load partition) with its intrinsic high strength. In addition, the strong elastic coupling with the dispersed pre-deformed interfacial martensite promotes the homogenization of stress-induced transformation. The composite of this hierarchy is primarily responsible for excellent elastocaloric cycling stability.
(3) The high lattice-match and strict crystallographic orientation of the nano-Ti_2Cu phase enable it reoriented reversibly in addition to the intrinsic elasticity upon loading, always keeping the fully coherent lattice with the transforming matrix. This ensures the epitaxial growth of the stress-induced transformation during elastocaloric cycling.
(4) In summary, the successful fabrication of NiTiCuCo alloy via LPBF not only fills the bill of its complex geometric structures for elastocaloric application, but refined microcomposite formed by the LPBF could exhibit novel performances that unachievable in traditional casting. An understanding of interphase coupling micro-behaviors could guide the designing additive manufactured SMAs on other functionalities.

Acknowledgments

This work was supported by National Key R&D Program of China (2022YFB4600500), the National Safety Academic Fund (U2130201 and U2330105) and the NSFC (52201214 and 51971244). The use of the Advanced Photon Source was supported by the US Department of Energy, Office of Science and Office of Basic Energy Science, under Contract No. DE-AC02-06CH11357.

Conflict of interest

The authors declare that they have no known competing financial interests or personal relationships that could have appeared to influence the work reported in this paper.

ORCID iD

Shijie Hao https://orcid.org/0000-0002-4427-851X

References

[1] Hou H L, Qian S X and Takeuchi I 2022 Materials, physics and systems for multicaloric cooling *Nat. Rev. Mater.* **7** 633–52
[2] Cong D Y *et al* 2019 Colossal elastocaloric effect in ferroelastic Ni-Mn-Ti alloys *Phys. Rev. Lett.* **122** 255703
[3] Qian S X, Geng Y L, Wang Y, Ling J Z, Hwang Y, Radermacher R, Takeuchi I and Cui J 2016 A review of elastocaloric cooling: materials, cycles and system integrations *Int. J. Refrig.* **64** 1–19
[4] Pataky G J, Ertekin E and Sehitoglu H 2015 Elastocaloric cooling potential of NiTi, Ni_2FeGa, and CoNiAl *Acta Mater.* **96** 420–7
[5] Qian S X, Catalini D, Muehlbauer J, Liu B Y, Mevada H, Hou H L, Hwang Y, Radermacher R and Takeuchi I 2023 High-performance multimode elastocaloric cooling system *Science* **380** 722–7
[6] Hou H L *et al* 2019 Fatigue-resistant high-performance elastocaloric materials made by additive manufacturing *Science* **366** 1116–21
[7] Bonnot E, Romero R, Mañosa L, Vives E and Planes A 2008 Elastocaloric effect associated with the martensitic transition in shape-memory alloys *Phys. Rev. Lett.* **100** 125901
[8] Hou H L, Simsek E, Stasak D, Hasan N A, Qian S X, Ott R, Cui J and Takeuchi I 2017 Elastocaloric cooling of additive manufactured shape memory alloys with large latent heat *J. Phys. D: Appl. Phys.* **50** 404001
[9] Yang Z, Cong D Y, Yuan Y, Li R G, Zheng H X, Sun X M, Nie Z H, Ren Y and Wang Y D 2020 Large room-temperature elastocaloric effect in a bulk polycrystalline Ni-Ti-Cu-Co alloy with low isothermal stress hysteresis *Appl. Mater. Today* **21** 100844
[10] Cissé C and Zaeem M A 2021 Design of NiTi-based shape memory microcomposites with enhanced elastocaloric performance by a fully thermomechanical coupled phase-field model *Mater. Des.* **207** 109898
[11] Cao Y X *et al* 2020 Large tunable elastocaloric effect in additively manufactured Ni–Ti shape memory alloys *Acta Mater.* **194** 178–89
[12] Ossmer H, Lambrecht F, Gültig M, Chluba C, Quandt E and Kohl M 2014 Evolution of temperature profiles in TiNi films for elastocaloric cooling *Acta Mater.* **81** 9–20
[13] Ding L, Zhou Y M, Xu Y Y, Dang P F, Ding X D, Sun J, Lookman T and Xue D Z 2021 Learning from superelasticity data to search for Ti-Ni alloys with large elastocaloric effect *Acta Mater.* **218** 117200
[14] Chen J Y, Liu B Q, Xing L L, Liu W, Lei L P and Fang G 2022 Toward tunable mechanical behavior and enhanced

elastocaloric effect in NiTi alloy by gradient structure *Acta Mater.* **226** 117609
[15] Gu H L, Bumke L, Chluba C, Quandt E and James R D 2018 Phase engineering and supercompatibility of shape memory alloys *Mater. Today* **21** 265–77
[16] Chluba C, Ge W W, De Miranda R L, Strobel J, Kienle L, Quandt E and Wuttig M 2015 Ultralow-fatigue shape memory alloy films *Science* **348** 1004–7
[17] Bumke L, Zamponi C, Jetter J and Quandt E 2020 Cu-rich $Ti_{52.8}Ni_{22.2}Cu_{22.5}Co_{2.5}$ shape memory alloy films with ultra-low fatigue for elastocaloric applications *J. Appl. Phys.* **127** 225105
[18] Ossmer H, Chluba C, Gueltig M, Quandt E and Kohl M 2015 Local evolution of the elastocaloric effect in TiNi-based films *Shape Mem. Superelasticity* **1** 142–52
[19] Bechtold C, Chluba C, De Miranda R L and Quandt E 2012 High cyclic stability of the elastocaloric effect in sputtered TiNiCu shape memory films *Appl. Phys. Lett.* **101** 091903
[20] Ahadi A, Ghorabaei A S, Shirazi H and Nili-Ahmadabadi M 2021 Bulk NiTiCuCo shape memory alloys with ultra-high thermal and superelastic cyclic stability *Scr. Mater.* **200** 113899
[21] Dang P F *et al* 2022 Low-fatigue and large room-temperature elastocaloric effect in a bulk $Ti_{49.2}Ni_{40.8}Cu_{10}$ alloy *Acta Mater.* **229** 117802
[22] Chen J Y, Lei L P and Fang G 2021 Elastocaloric cooling of shape memory alloys: a review *Mater. Today Commun.* **28** 102706
[23] Kirsch S M, Welsch F, Michaelis N, Schmidt M, Wieczorek A, Frenzel J, Eggeler G, Schütze A and Seelecke S 2018 NiTi-based elastocaloric cooling on the macroscale: from basic concepts to realization *Energy Technol.* **6** 1567–87
[24] Ishida A, Sato M and Ogawa K 2006 Microstructure and shape-memory behavior of annealed $Ti_{51.5}Ni_{33.1}Cu_{15.4}$ thin films *Phil. Mag. Lett.* **86** 13–20
[25] Meng X L, Sato M and Ishida A 2008 Structure of martensite in Ti-rich Ti-Ni-Cu thin films annealed at different temperatures *Acta Mater.* **56** 3394–402
[26] Ishida A, Sato M and Gao Z Y 2014 Effects of Ti content on microstructure and shape memory behavior of $TixNi_{(84.5-x)}Cu_{15.5}$ ($x = 44.6$–55.4) thin films *Acta Mater.* **69** 292–300
[27] Lu H Z *et al* 2022 Simultaneous enhancement of mechanical and shape memory properties by heat-treatment homogenization of Ti_2Ni precipitates in TiNi shape memory alloy fabricated by selective laser melting *J. Mater. Sci. Technol.* **101** 205–16
[28] Wang J C, Zhu R, Liu Y J and Zhang L C 2023 Understanding melt pool characteristics in laser powder bed fusion: an overview of single- and multi-track melt pools for process optimization *Adv. Powder Mater.* **2** 100137
[29] Wei S S, Zhang J L, Zhang L, Zhang Y J, Song B, Wang X B, Fan J X, Liu Q and Shi Y S 2023 Laser powder bed fusion additive manufacturing of NiTi shape memory alloys: a review *Int. J. Extreme Manuf.* **5** 032001
[30] Chen W, Gu D D, Yang J K, Yang Q, Chen J and Shen X F 2022 Compressive mechanical properties and shape memory effect of NiTi gradient lattice structures fabricated by laser powder bed fusion *Int. J. Extreme Manuf.* **4** 045002
[31] Zhang C, Zhu J K, Zheng H, Li H, Liu S and Cheng G J 2020 A review on microstructures and properties of high entropy alloys manufactured by selective laser melting *Int. J. Extreme Manuf.* **2** 032003
[32] Wei C, Zhang Z Z, Cheng D X, Sun Z, Zhu M H and Li L 2021 An overview of laser-based multiple metallic material additive manufacturing: from macro- to micro-scales *Int. J. Extreme Manuf.* **3** 012003
[33] Ren J *et al* 2022 Strong yet ductile nanolamellar high-entropy alloys by additive manufacturing *Nature* **608** 62–68
[34] Ren J *et al* 2023 Deformation mechanisms in an additively manufactured dual-phase eutectic high-entropy alloy *Acta Mater.* **257** 119179
[35] Guo Y N, Su H J, Zhou H T, Shen Z L, Liu Y, Zhang J, Liu L and Fu H Z 2022 Unique strength-ductility balance of $AlCoCrFeNi_{2.1}$ eutectic high entropy alloy with ultra-fine duplex microstructure prepared by selective laser melting *J. Mater. Sci. Technol.* **111** 298–306
[36] Zhu Y M *et al* 2022 Ultrastrong nanotwinned titanium alloys through additive manufacturing *Nat. Mater.* **21** 1258–62
[37] Guo W Q, Feng B, Yang Y, Ren Y, Liu Y N, Yang H, Yang Q, Cui L S, Tong X and Hao S J 2022 Effect of laser scanning speed on the microstructure, phase transformation and mechanical property of NiTi alloys fabricated by LPBF *Mater. Des.* **215** 110460
[38] Feng B, Wang C, Zhang Q Q, Ren Y, Cui L S, Yang Q and Hao S J 2022 Effect of laser hatch spacing on the pore defects, phase transformation and properties of selective laser melting fabricated NiTi shape memory alloys *Mater. Sci. Eng.* A **840** 142965
[39] Ma H Y, Wang J C, Qin P, Liu Y J, Chen L Y, Wang L Q and Zhang L C 2024 Advances in additively manufactured titanium alloys by powder bed fusion and directed energy deposition: microstructure, defects, and mechanical behavior *J. Mater. Sci. Technol.* **183** 32–62
[40] Wang X B *et al* 2020 Effect of process parameters on the phase transformation behavior and tensile properties of NiTi shape memory alloys fabricated by selective laser melting *Addit. Manuf.* **36** 101545
[41] Bakhtiari S, Li Y C, Sarkar S, Yang H, Cui L S and Liu Y N 2022 Deformation induced martensite stabilization of NiTi in constrained composite systems *Mater. Sci. Eng.* A **857** 144128
[42] Liu Z Y, Cui L S, Liu Y N, Jiang D Q, Jiang J, Shi X B, Shao Y and Zheng Y J 2014 Influence of internal stress coupling on the deformation behavior of NiTi-Nb nanowire composites *Scr. Mater.* **77** 75–78
[43] Feng B *et al* 2020 *In-situ* synchrotron high energy x-ray diffraction study of micro-mechanical behaviour of R phase reorientation in nanocrystalline NiTi alloy *Acta Mater.* **194** 565–76
[44] Kong X G, Hao S J, Ren Y, Yang Y, Feng B, Guo F M, Yang Q, Huang B M and Cui L S 2022 Interactions between martensitic NiTi shape memory alloy and Nb nanowires in composite wire during tensile deformation *Composites* B **234** 109690
[45] Li Y F, Tang S L, Gao Y M, Ma S Q, Zheng Q L and Cheng Y H 2017 Mechanical and thermodynamic properties of intermetallic compounds in the Ni-Ti system *Int. J. Mod. Phys.* B **31** 1750161
[46] Zhang J S, Hao S J, Jiang D Q, Huan Y, Cui L S, Liu Y N, Yang H and Ren Y 2017 In situ synchrotron high-energy x-ray diffraction study of microscopic deformation behavior of a hard-soft dual phase composite containing phase transforming matrix *Acta Mater.* **130** 297–309
[47] Hao S J, Cui L S, Ren Y, Han X D *et al* 2013 A transforming metal nanocomposite with large elastic strain, low modulus, and high strength *Science* **339** 1191–4
[48] Zhang J S, Liu Y N, Ren Y, Huan Y, Hao S J, Yu C, Shao Y, Ru Y D, Jiang D Q and Cui L S 2014 *In situ* synchrotron x-ray diffraction study of deformation behavior and load transfer in a Ti_2Ni-NiTi composite *Appl. Phys. Lett.* **105** 041910
[49] Zhu Z G, Ng F L, Seet H L, Lu W J, Liebscher C H, Rao Z Y, Raabe D and Nai S M L 2022 Superior mechanical properties of a selective-laser-melted AlZnMgCuScZr alloy enabled by a tunable hierarchical microstructure and dual-nanoprecipitation *Mater. Today* **52** 90–101

[50] Wang J C, Liu Y J, Liang S X, Zhang Y S, Wang L Q, Sercombe T B and Zhang L C 2022 Comparison of microstructure and mechanical behavior of Ti-35Nb manufactured by laser powder bed fusion from elemental powder mixture and prealloyed powder *J. Mater. Sci. Technol.* **105** 1–16

[51] Martin J H, Yahata B D, Hundley J M, Mayer J A, Schaedler T A and Pollock T M 2017 3D printing of high-strength aluminium alloys *Nature* **549** 365–9

[52] Sui S, Chew Y, Weng F, Tan C L, Du Z L and Bi G J 2022 Study of the intrinsic mechanisms of nickel additive for grain refinement and strength enhancement of laser aided additively manufactured Ti-6Al-4V *Int. J. Extreme Manuf.* **4** 035102

[53] Pan X Y and Qiu C L 2022 Promoting columnar-to-equiaxed transition in AlCoCrFeNi high entropy alloy during selective laser melting by adding Cr_3C_2 *Mater. Res. Lett.* **10** 788–96

[54] Chokshi A H, Rosen A, Karch J and Gleiter H 1989 On the validity of the hall-petch relationship in nanocrystalline materials *Scr. Metall.* **23** 1679–83

[55] Furukawa M, Horita Z, Nemoto M, Valiev R Z and Langdon T G 1996 Microhardness measurements and the Hall-Petch relationship in an Al Mg alloy with submicrometer grain size *Acta Mater.* **44** 4619–29

[56] Nieh T G and Wadsworth J 1991 Hall-petch relation in nanocrystalline solids *Scr. Metall. Mater.* **25** 955–8

[57] Zhang J S, Hao S J, Jiang D Q, Huan Y, Cui L S, Liu Y N, Ren Y and Yang H 2018 Dual phase synergy enabled large elastic strains of nanoinclusions in a dislocation slip matrix composite *Nano Lett.* **18** 2976–83

[58] Pelton A R 2011 Nitinol fatigue: a review of microstructures and mechanisms *J. Mater. Eng. Perform.* **20** 613–7